A single-image retrieval method for edge illumination X-ray phase-contrast imaging: application and noise analysis

Paul C. Diémoz[a,b,*], Fabio A. Vittoria[a,b], Charlotte K. Hagen[a], Marco Endrizzi[a], Paola Coan[c,d], Alberto Bravin[e], Ulrich H. Wagner[f], Christoph Rau[f], Ian K. Robinson[b,g] and Alessandro Olivo[a,b]

[a]*Department of Medical Physics and Biomedical Engineering, University College London, London, UK*
[b]*Research Complex at Harwell, Oxford Harwell Campus, Didcot, UK*
[c]*Institute for Clinical Radiology, Ludwig-Maximilians-University, Munich, Germany*
[d]*Department of Physics, Ludwig-Maximilians-University, Garching, Germany*
[e]*European Synchrotron Radiation Facility, Grenoble, France*
[f]*Diamond Light Source, Harwell Oxford Campus, Didcot, UK*
[g]*London Centre for Nanotechnology, London, UK*

*Correspondence e-mail: p.diemoz@ucl.ac.uk

Abstract

Purpose: Edge illumination (EI) X-ray phase-contrast imaging (XPCI) has been under development at University College London in recent years, and has shown great potential for both laboratory and synchrotron applications. In this work, we propose a new acquisition and processing scheme. Contrary to existing retrieval methods for EI, which require as input two images acquired in different setup configurations, the proposed approach can retrieve an approximate map of the X-ray phase from a single image, thus significantly simplifying the acquisition procedure and reducing data collection times.

Methods: The retrieval method is analytically derived, based on the assumption of a quasi-homogeneous object, i.e. an object featuring a constant ratio between refractive index and absorption coefficient. The noise properties of the input and retrieved images are also theoretically analyzed under the developed formalism. The method is applied to experimental synchrotron images of a biological object.

Results: The experimental results show that the method can provide high-quality images, where the "edge" signal typical of XPCI images is transformed to an "area" contrast that enables an easier interpretation of the sample geometry. Moreover, the retrieved images confirm that the method is highly stable against noise.

Conclusions: We anticipate that the developed approach will become the method of choice for a variety of applications of EI XPCI, thanks to its ability to simplify the acquisition procedure and reduce acquisitions time and dose to the sample. Future work will focus on the adaptation of the method to computed tomography and to polychromatic radiation from X-ray tubes.

Key words: phase-contrast imaging, edge illumination, fast imaging, phase retrieval

1. Introduction

Edge illumination (EI) is an X-ray phase-contrast imaging (XPCI) technique that is currently being developed at University College London [1,2]. As opposed to conventional imaging techniques, in XPCI the contrast does not only rely on the absorption of the sample, but is also produced by the phase shift that X-rays experience when passing through different regions of the sample [3,4]. This new mechanism for generating contrast can provide images with considerably improved detail visualization, especially in the case of materials with similar attenuation properties, such as biological soft tissues. The phase shift undergone by the beam, in fact, can be significant even when its absorption counterpart is very small and insufficient to create adequate image contrast.

EI has been extensively applied using both monochromatic synchrotron radiation [1,5-8] and polychromatic and divergent beams generated by X-ray tubes [2,9-13]. In particular, the applicability to X-ray tubes in table-top laboratory setups is possible thanks to the low coherence requirements of the technique, both in terms of beam polychromaticity and focal spot size [2,10,14,15]. This feature of EI has the potential to enable a widespread implementation of the technique for various applications in fields like biology, medicine, industrial testing, etc.

A schematic of the EI working principle is presented in Fig. 1. The beam is collimated before the sample by means of a slit (henceforth called "sample slit", with an aperture of a few or tens of μm) and the beamlet exiting the object is then analyzed by means of a second slit (the "detector slit"), placed in front of the detector and aligned with a line of detector pixels. The two slits are misaligned with respect to each other, so that a fraction of the beamlet is stopped by the detector slit, while the remaining part is directly incident onto the detector (Fig. 1a). The presence of the sample in the beam can have two effects. It can attenuate the beam intensity, thus reducing the signal on the detector, and it can refract the beam, thus changing its direction of propagation (Fig. 1b). By placing the detector at a certain distance from the sample, this deviation is converted into a spatial displacement of the beam, given by $\Delta y = z_{od} \cdot \Delta\theta_y$, where z_{od} is the object-to-detector distance and $\Delta\theta_y$ is the refraction angle in the direction orthogonal to the slit aperture. This has the effect of increasing or decreasing the amount of photons hitting the detector, depending on the direction of refraction (Fig. 1b). An image of the sample can be obtained by scanning the object through the beam, and recording the detector signal at each step of the scan. When using wide beams produced by X-ray tubes, however, this scan can be avoided by replacing the two slits with two masks featuring several apertures, thus replicating the EI principle over the whole extent of the object [2,9,10].

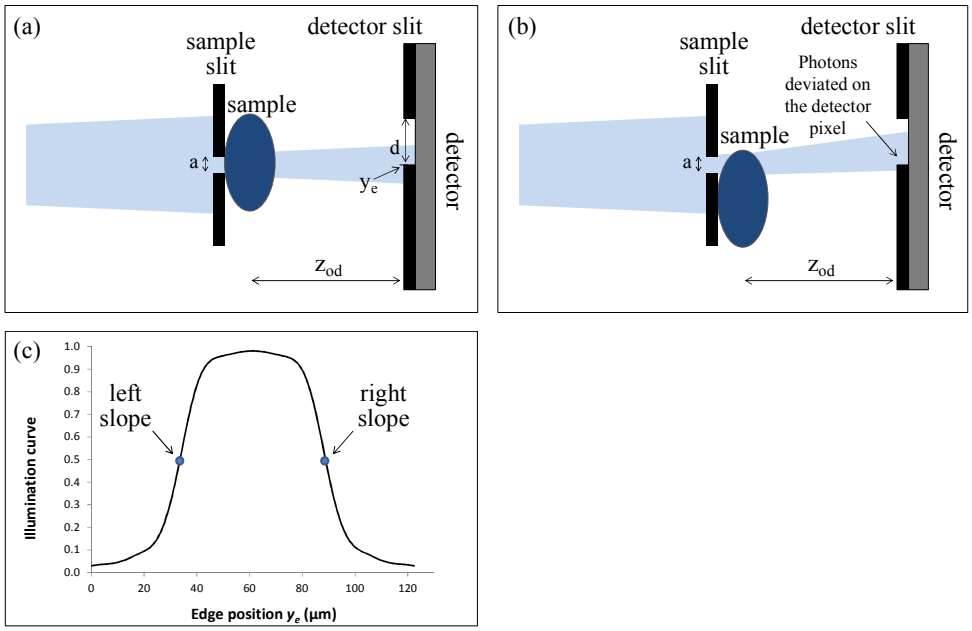

Figure 1. Schematic diagram of the EI principle. (a) Sample and detector slits are misaligned with respect to each other, so that part of the beam is stopped by the detector slit, while the remaining part is incident on a line of detector pixels (oriented in the direction orthogonal to the plane of drawing). (b) When the sample is inserted, in addition to attenuating the beam, it can deviate the photons on (or out of) the detector, thus increasing (or decreasing) the recorded intensity. (c) Example of illumination curve.

We will consider in the following the case of a parallel and monochromatic beam (synchrotron case). If the direction x parallel to the mask lines is for the moment neglected, the signal measured on the detector at object position p can be expressed as [7,10]:

$$S(p) = N \cdot T(p) C\left(y_e - z_{od} \cdot \Delta\theta_y(p)\right) \tag{1}$$

where N is the number of photons passing through the sample slit and $T(p) = \exp\left(-\int dz \mu(p,z)\right)$ is the beam transmission through the sample, with μ the linear attenuation coefficient. $C(y_e)$ is the so-called illumination curve (shown in Fig. 1c), which represents the fraction of photons passing through the detector slit, as a function of the misalignment y_e between the slits. Values of $C(y_e)$ range from about 0 (when the slits are totally misaligned) to about 1 (when the slits are perfectly aligned). In Eq. 1, the argument of the illumination curve is shifted by $-z_{od} \cdot \Delta\theta_y(y)$. This is because a displacement of the beam caused by refraction is, from the point of view of the signal, perfectly equivalent to a displacement of the detector slit in the opposite direction. The refraction angle is given by $\Delta\theta_y(p) = k^{-1} \partial\phi/\partial y(p)$, where k is the wavenumber, $\phi(p) = -k\int dz \delta(p,z)$ is the phase shift and δ is the refractive index. Due to its differential nature, the refraction signal mainly originates at the boundaries of the various object structures.

As can be seen from Eq. 1, the image signal depends on both the transmission and phase shift. Therefore, if these two object properties need to be separated and quantified, the acquisition and subsequent processing of two images, acquired in different configurations of the setup, is usually required. From a mathematical perspective, in fact, two equations are needed in order to retrieve the two unknowns T and ϕ. In practice, retrieval for EI is normally carried out by

acquiring two images on the left and right slopes of the function *C* (Fig. 1c) [7,10]. This corresponds to taking two images with the detector slit stopping either the lower or the upper part of the beam.

This retrieval method has been demonstrated to extract accurate attenuation and phase information, both in laboratory [10,13] and synchrotron [7] EI setups. However, this procedure is not ideal if fast acquisitions are needed or in the case of computed tomography, as every image acquisition needs to be repeated twice at two different slit misalignments.

In the next section, a new acquisition and retrieval method that requires only a single input image is described, and in section 3 this method is applied to an experimental image acquired using synchrotron radiation.

2. Theory

In the following derivation, we make the assumption that the refraction angles produced by the sample are small, so that a linear approximation can be safely adopted for the illumination curve on one of its slopes (c.f. Eq. 1 and Fig. 1c). Moreover, we exploit the fact that, in the direction parallel to the slits, the signal is equal to the free-space propagation (FSP) one, i.e. the one that would be obtained without the presence of the slits [16]. The latter can be expressed using the well-known transport-of-intensity (TIE) equation, in the approximation of near-field regime [17,18]:

$$S(x) = T(x) * LSF_x(x) - k^{-1} z_{od} \nabla_x \left[T(x) \nabla_x \phi(x) \right] * LSF_x(x) \tag{2}$$

where LSF_x is the line-spread function of the detector along *x*, and ∇_x indicates the spatial derivative along the same direction. Combining the signals in the two directions *x* and *y*, we obtain, for the normalized signal [19]:

$$S_n(x,p) = T(x,p) * LSF_x(x) - T(x,p) \frac{C'(y_e)}{C(y_e)} k^{-1} z_{od} \nabla_y \phi(x,p) - k^{-1} z_{od} \nabla_x \left[T(x,p) \nabla_x \phi(x,p) \right] * LSF_x(x) \tag{3}$$

where $C'(y_e)$ is the first derivative of the illumination curve; $S_n(x,p) \equiv S(x,p) / NC(y_e)$, and $NC(y_e)$ represents the number of counts when the object is not in the beam. The second term on the right-hand side of Eq. 3 corresponds to the EI signal along *y*, while the third one corresponds to the FSP one along *x*. A detailed comparison of the amplitude of the EI and FSP signals in the two directions, as a function of the setup parameters, can be found in [20].

We now assume that the ratio $\gamma = \delta(t) / \mu(t)$ is approximately constant within the object, so that $\phi = -k\gamma \int dt \mu(t)$. This is the same assumption adopted by the so-called Paganin algorithm [21], and used by the algorithms proposed in [22,23], which has been shown to hold in numerous practical cases, in particular for the imaging of soft biological tissues. Eq. 3 can then be rewritten as:

$$S_n = \exp\left(-\int dt \mu\right) * LSF_x + \gamma J_{EI} \exp\left(-\int dt \mu\right) \nabla_y \int dt \mu + \gamma z_{od} \nabla_x \left[\exp\left(-\int dt \mu\right) \nabla_x \int dt \mu \right] * LSF_x \tag{4}$$

where, for simplicity of notation, we have discarded the dependences upon positions x and p, and where we have defined $J_{EI} \equiv z_{od}\, C'(y_e)/C(y_e)$. By noting that $\exp\left(-\int dt\,\mu\right)\nabla_{x,y}\int dt\,\mu = -\nabla_{x,y}\exp\left(-\int dt\,\mu\right)$, we can write:

$$S_n = \left(LSF_x * -\gamma J_{EI}\nabla_y - \gamma z_{od} LSF_x * \nabla_x^2\right)\exp\left(-\int dt\,\mu\right) \tag{5}$$

By taking the Fourier transform of both sides of Eq. 5, we get:

$$F\{S_n\} = \left(MTF_x(f_x) - 2\pi i\gamma J_{EI} f_y + 4\pi^2\gamma z_{od} MTF_x(f_x)\cdot f_x^2\right)\cdot F\left\{\exp\left(-\int dt\,\mu\right)\right\} \tag{6}$$

where f_x and f_y are the spatial frequencies along x and y, and $MTF_x(f_x) \equiv F\{LSF_x\}$ is the detector modulation transfer function along x. Therefore, we have demonstrated that the measured intensity is equal to a filtered version of the ideal "contact" image (i.e. the image that would be measured with an ideal detector and no propagation distance between sample and detector). This contact image can then be retrieved as [19]:

$$\exp\left(-\int dt\,\mu\right) = F^{-1}\left\{\frac{F\{S_n\}}{MTF_x(f_x) - 2\pi i\gamma J_{EI} f_y + 4\pi^2\gamma z_{od} MTF_x(f_x)\cdot f_x^2}\right\} \tag{7}$$

and, remembering the relationship between the object phase and absorption, the phase shift map can be calculated as:

$$\phi = \gamma\log\left[F^{-1}\left\{\frac{F\{S_n\}}{MTF_x(f_x) - 2\pi i\gamma J_{EI} f_y + 4\pi^2\gamma z_{od} MTF_x(f_x)\cdot f_x^2}\right\}\right] \tag{8}$$

Therefore, contact image and phase shift map can be obtained simply by appropriate filtering in Fourier space of the measured EI image.

Following the approach used in [24], it is also possible to analyse the noise properties of this algorithm. In fact, it can be shown that, if an image is filtered in Fourier space using a given filter $filt(f_x, f_y)$, the noise power spectrum (NPS) of the resulting image is equal to the NPS of the original image multiplied by $\left|filt(f_x, f_y)\right|^2$ [24,25]. In our specific case, this means that the NPSs of the measured EI image and retrieved contact image are related by:

$$NPS_{contact}(f_x, f_y) = \frac{NPS_{EI}(f_x, f_y)}{\left[MTF_x(f_x) + 4\pi^2\gamma z_{od} MTF_x(f_x)\cdot f_x^2\right]^2 + \left[2\pi\gamma J_{EI} f_y\right]^2} \tag{9}$$

We will not investigate here the absolute noise properties of the input EI image and of the retrieved contact image, as these will be given, in general, by a combination of statistical Poissonian noise (determined by limited photon statistics) and of experimental noise, which could include slits non-uniformity, beam instability, detector read-out noise, etc. Instead, we are interested in determining how the noise in the input image is transferred to the retrieved image through the considered filter. In order to do so, in the next section we will investigate the value of the filter in Eq. 9 as a function of the spatial frequencies f_x and f_y, in the case of the parameters used in our experimental synchrotron setup. Alongside this, we will present an example of application of the single-image retrieval algorithm to experimental images.

3. Experimental results

An experimental verification of the proposed algorithm was carried out on EI images acquired using synchrotron radiation. The sample was a slice of bamboo wood, approximately 500 μm thick. The experiment was performed at the I13 beamline (coherence branch) of the Diamond synchrotron radiation facility (Didcot, UK), using an energy of 9.7 keV. The beam was collimated using a slit of 3 μm aperture, oriented horizontally and made of gold electroplated on a silicon substrate. The slit-to-sample distance was 5 cm, and the sample-to-detector distance was 30 cm. The detector was a PCO Edge camera, consisting of a scintillator, magnifying visible light optics and a sCMOS sensor, with an effective pixel size at the sample plane of 0.8 μm. In this experiment, the so-called "virtual edge" EI configuration was employed [8], whereby no detector slit is physically present. Instead, thanks to the high resolution of the detector, a virtual edge is created by multiplying the acquired frame by a Heaviside function, so as to select half of the pixels along the vertical direction [8]. A scan of the sample with a 1.6 μm step was performed. The average number of counts for each pixel in the final image was around 1100, in a region outside of the sample.

First, we analyse the shape of the Fourier filter in the case of our experimental setup, in order to determine its properties in terms of noise propagation. We present, in Fig. 2a, an image of the filter $1\Big/\left[MTF_x\left(f_x\right)+4\pi^2\gamma z_{od}MTF_x\left(f_x\right)\cdot f_x^2\right]^2+\left[2\pi\gamma J_{EI}f_y\right]^2$. An enlarged version of the ROI indicated in Fig. 2a by the dashed red square is also shown in Fig. 2b (note the very different color scales used for the two images). To calculate the filter function, we considered a value of $\delta/\mu = 4.21\cdot10^{-9}$ m, corresponding to water at 9.7 keV [26]. Moveover, we assumed that the LSF of the used detector was equal to a rectangular function of 0.8 μm width convolved with a Gaussian function of 0.4 μm standard deviation. Note that the maximum frequencies along x and y are different, as they are equal to $1\Big/\left(2\,pixel\right)$ and $1\Big/\left(2step\right)$, respectively, where the scan step of 1.6 μm along y is larger than the 0.8 μm pixel size.

In Figs. 2c and 2d, we show horizontal and vertical profiles of the filter function, indicated by the dashed lines in Fig. 2b. They correspond to lines $f_y = 0$ and $f_x = 0$, respectively, and have been chosen to show the dependency upon the frequencies along x and y. The different shape of the filter in the two directions is given by the different dependency upon f_x and f_y (c.f. Eq. 8). As can be seen, this is a low-pass filter, which has the effect of significantly damping the high-frequency components in the image. As a result, we expect the algorithm to be stable with respect to high frequency noise in the image. At the same time, the value of the filter never diverges at low frequencies (it is comprised between 0 and 1), and therefore we expect it to be also well-behaved at low frequencies.

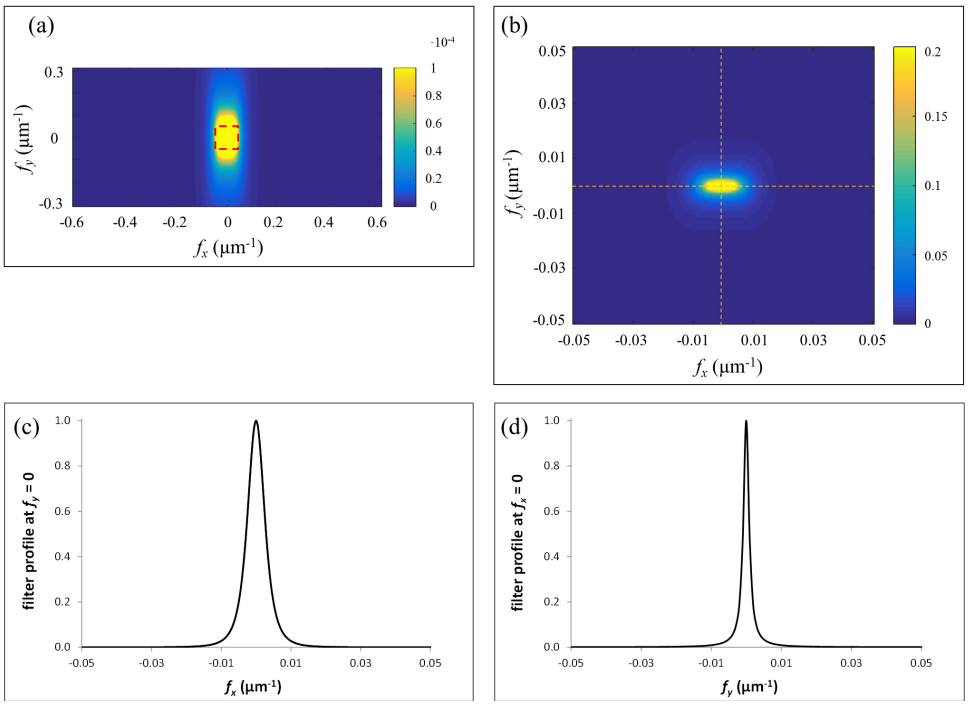

Figure 2. (a) Image of the Fourier filter used by Eq. 8. (b) Enlarged view of the region indicated by the dashed red square in (a). (c) Profile along the horizontal line in (b). (d) Profile along the vertical line in (b).

The EI image of the bamboo sample is shown in Fig. 3a, and the retrieved contact image in Fig. 3b. The retrieved image does not contain the line artefacts that typically arise when the phase is obtained from integration of the refraction image [27]. As expected from the analysis of the filter discussed above (see Fig. 2), the algorithm also appears to be stable with respect to high-frequency noise. It should also be noted that the two images have a different appearance. The EI image in Fig. 3a contains a mixture of transmission and phase contrast, the latter mainly localised at the boundaries of the various structures. In the retrieved one, this "edge" contrast is transformed into a conventional "area" contrast, which enables a simpler interpretation of the sample features. This is quite evident in the enlarged views of a region within the sample presented in Figs. 3c and 3d. In particular, the fibrous structure of the wood can be much better appreciated in the retrieved contact image. As a further comparison, the refraction angle map for the same region of the sample, extracted using the conventional 2-image retrieval algorithm for EI [7], is shown in Fig. 3e. Also with respect to the latter, the retrieved contact image proves superior in terms of clear visualization of the sample geometry.

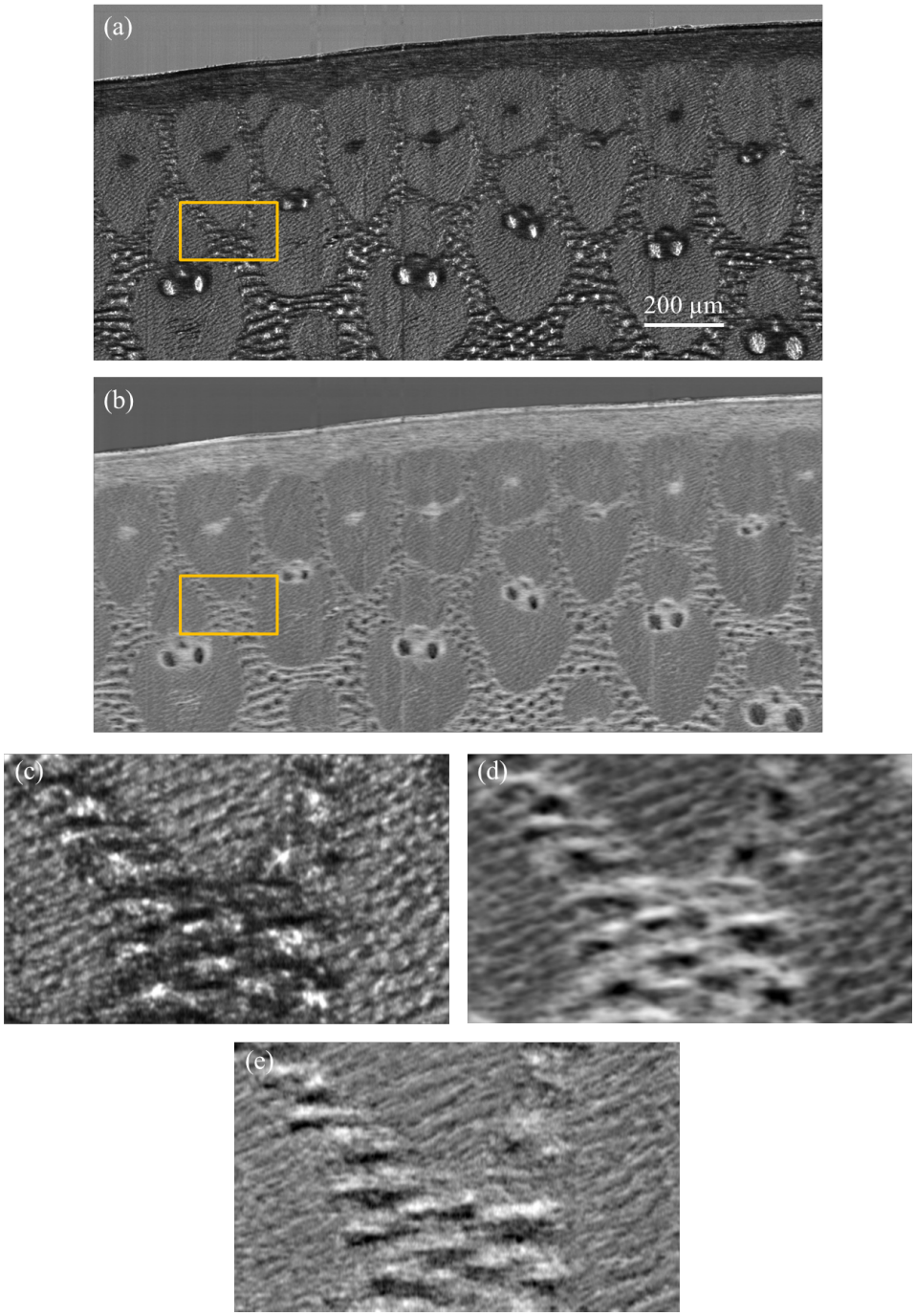

Figure 3. (a) EI image of a slice of bamboo wood. (b) Retrieved contact image calculated from EI image in (a). (c) Enlarged view of area indicated by the rectangle in (a). (d) Enlarged view of area indicated by the rectangle in (b). (e) Refraction angle map extracted using the conventional 2-image retrieval algorithm, for the same sample region considered in (c) and (d).

4. Conclusions

We have developed a new method for phase retrieval in the EI XPCI technique, which requires the acquisition and mathematical processing of a single input image. This represents a key advantage with respect to the retrieval method commonly used for EI [7,10], where the acquisition of two images of the sample at two different slit misalignments is needed. The requirement of a single image greatly simplifies the experimental procedure, as the mechanical movement of one of the slits during image collection is avoided. Thus, it enables a reduction of acquisition times and of the radiation dose delivered to the sample. In particular, if applied in combination with computed tomography, this method will allow performing a continuous rotation of the sample, as only one image per angle view is needed.

We have described the physical assumptions made by the algorithm, and investigated its noise properties. Since the algorithm basically consists in a low-pass filter, it reduces the high-frequency noise in the retrieved image. This can enable dose reduction strategies, as even high noise in the input image due to limited photon statistics could be tolerated. The algorithm assumes the case of near-field regime, in order for the TIE to be valid. Thus, it may lose some accuracy if large propagation distances are used to increase the image contrast. In order to preserve the accuracy of the algorithm outside the near-field regime, one could potentially modify the Fourier filter in the FSP direction, for instance along the lines of the algorithms proposed by Gureyev et al [28] and Hofmann et al [29]. The method has been experimentally verified using synchrotron radiation. Not only does it produce an artefact-free retrieved image, but it also enables an improved visualization of the sample structures, since the "edge signal" typical of EI images is directly transformed into an "area signal" that is more easily interpreted.

Acknowledgments

This work was supported by the UK Engineering and Physical Sciences Research Council (Grants EP/I021884/1 and EP/I022562/1). PCD is supported by a Marie Curie Career Integration Grant PCIG12-GA-2012-333990 within the Seventh Framework Programme of the European Union.

References

[1] Olivo A, Arfelli F, Cantatore G, Longo R, Menk R, Pani S, et al. An innovative digital imaging set-up allowing a low-dose approach to phase contrast applications in the medical field. Med Phys 2001;28(8):1610-19.

[2] Olivo A, Speller RD. A coded-aperture technique allowing x-ray phase contrast imaging with conventional sources. Appl Phys Lett 2007;91(7): 074106.

[3] Bravin A, Coan P, Suortti P. X-ray phase-contrast imaging: from pre-clinical applications towards clinics. Phys Med Biol 2013;58:R1–R35.

[4] Wilkins SW, Nesterets YI, Gureyev T E, Mayo SC, Pogany A, Stevenson AW. On the evolution and relative merits of hard X-ray phase-contrast imaging methods. Philos Trans R Soc A 2014;372:20130021.

[5] Olivo A,Bohndiek SE, Griffiths JA, Konstantinidis A, Speller RD. A non-free-space propagation x-ray phase contrast imaging method sensitive to phase effects in two directions simultaneously. Appl Phys Lett 2009;94:044108.

[6] Olivo A, Diemoz PC, Bravin A. Amplification of the phase contrast signal at very high x-ray energies. Opt Lett 2012;37(5): 915-7.

[7] Diemoz PC, Endrizzi M, Zapata CE, Pešić ZD, Rau C, Bravin A, et al. X-ray phase-contrast imaging with nanoradian angular resolution. Phys Rev Lett 2013;110(13):138105.

[8] Vittoria FA, Endrizzi M, Diemoz PC, Wagner UH, Rau C, Robinson IK, et al. Virtual edge illumination and one dimensional beam tracking for absorption, refraction, and scattering retrieval. Appl Phys Lett 2014;104:134102.

[9] Munro PRT, Ignatyev K, Speller RD, Olivo A. Phase and absorption retrieval using incoherent X-ray sources. Proc Natl Acad Sci USA 2012;109(35):13922.

[10] Diemoz PC, Hagen CK, Endrizzi M, Olivo A. Sensitivity of laboratory based implementations of edge illumination X-ray phase-contrast imaging. Appl Phys Lett 2013;103(24):244104.
[11] Olivo A, Gkoumas S, Endrizzi M, Hagen CK, Szafraniec MB, Diemoz PC, et al. Low-dose phase contrast mammography with conventional x-ray sources. Med Phys 2013;40(9):090701.
[12] Endrizzi M, Diemoz PC, Millard TP, Jones JL, Speller RD, Robinson IK, et al. Hard X-ray dark-field imaging with incoherent sample illumination. Appl Phys Lett 2014;104(2):024106.
[13] Hagen CK, Munro PRT, Endrizzi M, Diemoz PC, Olivo A. Low-dose phase contrast tomography with conventional x-ray sources. Med Phys 2014;41:070701.
[14] Diemoz PC, Olivo A. On the origin of contrast in edge illumination X-ray phase-contrast imaging. Opt Express 2014;22(23):28199-214.
[15] Endrizzi M, Vittoria FA, Kallon G, Basta D, Diemoz PC, Vincenzi A, et al. Achromatic approach to phase-based multi-modal imaging with conventional X-ray sources. Opt Express 2015;23(12):16473-80.
[16] Diemoz PC, Vittoria FA, Olivo A. Spatial resolution of edge illumination X-ray phase-contrast imaging. Opt Express 2014;22(13):15514–29.
[17] Teague MR. Deterministic phase retrieval: a Green's function solution. J Opt Soc Am 1983;73(11):1434–41.
[18] Gureyev TE, Nesterets YI, Stevenson AW, Miller PR, Pogany A, Wilkins SW. Some simple rules for contrast, signal-to-noise and resolution in in-line x-ray phase-contrast imaging. Opt Express 2008;16(5):3223–41.
[19] Diemoz PC, Vittoria FA, Hagen CK, Endrizzi M, Coan P, Brun E, et al. Single-image phase retrieval using an edge illumination X-ray phase-contrast imaging setup. J Synchron Radiat 2015;22:1072–7.
[20] Diemoz PC, Vittoria FA, Olivo A. Concept of contrast transfer function for edge illumination x-ray phase-contrast imaging and its comparison with the free-space propagation technique. Opt Express 2016;24(10):11250-65.
[21] Paganin D, Mayo SC, Gureyev TE, Miller PR, Wilkins SW. Simultaneous phase and amplitude extraction from a single defocused image of a homogeneous object. J Microsc 2002;206(1):33–40.
[22] Pavlov KM, Gureyev TE, Paganin D, Nesterets YI, Morgan MJ, Lewis RA. Linear systems with slowly varying transfer functions and their application to x-ray phase-contrast imaging. J Phys D 2004;37:2746–50.
[23] Briedis D, Siu KKW, Paganin DM, Pavlov KM, Lewis RA. Analyser-based mammography using single-image reconstruction. Phys Med Biol 2005;50:3599–3611.
[24] Nesterets YI, Gureyev TE. Noise propagation in x-ray phase-contrast imaging and computed tomography. J Phys D: Appl Phys 2014;47(10):105402.
[25] Barrett HH, Myers KJ. Foundations of Image Science. Hoboken, NJ: Wiley; 2004.
[26] Dejus RJ, Sanchez del Rio M. XOP: A graphical user interface for spectral calculations and x-ray optics utilities. Rev Sci Instrum 1996;67(9):3356.
[27] Thüring T, Modregger P, Pinzer BR, Wang Z, Stampanoni M. Non-linear regularized phase retrieval for unidirectional X-ray differential phase contrast radiography. Opt Express 2011;19(25):25545–58.
[28] Gureyev TE, Pogany A, Paganin DM, Wilkins SW. Linear algorithms for phase retrieval in the Fresnel region. Opt Commun 2004;231:53–70.
[29] Hofmann R, Schober A, Hahn S, Moosmann J, Kashef J, Hertel M, et al. Gauging low-dose X-ray phase-contrast imaging at a single and large propagation distance. Opt Express 2016;24(4):4331-48.